

# Multiplex optical biosensors based on multi-pinhole interferometry

JOHANNES BLÄSI\*  AND MARTINA GERKEN 

*Institute of Electrical Engineering and Information Technology, Kiel University, Kaiserstraße 2, 24143 Kiel, Germany*

*\*jbl@tf.uni.kiel.de*

**Abstract:** The application of new sensor technologies for frequent biomarker monitoring in combination with the leverage of artificial intelligence has great potential to improve the design and safety of health care. With current research efforts, the screening of tens of biomarkers at the point of care and immediate adjustment of therapy is coming within reach. Here we introduce an optical multiplexing approach based on multi-pinhole interference providing inherent differential referencing between a multitude of measurement fields on a surface. A theoretical study of an 11-plex and a 54-plex design is complemented with the experimental demonstration of the technique for a 3-field refractive index measurements and detection of human  $\alpha$ -thrombin.

© 2021 Optical Society of America under the terms of the [OSA Open Access Publishing Agreement](#)

## 1. Introduction

Improving health care requires the screening of multiple molecular biomarkers combined with artificial intelligence for prediction of diseases [1–3]. The current gold standard methods for molecular biomarker screening in body fluids include polymerase chain reaction (PCR) or enzyme-linked immunosorbent assays (ELISA). Both are typically not available at the point of care (PoC). For personal use single-parameter tests such as pregnancy tests or recently SARS-CoV-2 tests are widely available. The current research aim is to develop miniaturized measurement systems for the evaluation of biomarker panels with a limit of detection (LOD) on the order of 1 pg/ml. To increase predictive power sampled body fluids should be screened regarding a multitude of molecular biomarkers in parallel. For example, for cancer screening the measurement of at least 4–10 biomarkers is recommended [4]. Recently, progress in screening tens of biomarkers at the point of care has been shown [2–11]. Electrochemical biosensors based on amperometry [6], potentiometric or field-effect transistors [7,8] show low LODs, and rapid label-free biomarker detection. Field-effect transistor-based biosensors allow direct low LOD multiplex biomarker measurements [7,8]. Optical nanomechanical cantilevers show multiplex microRNA detection at low concentrations [9]. Localized surface plasmon resonance sensors are already applied for label-free, multiplex, and real time analysis of cytokines in low concentrations [10]. Micro-ring resonator arrays are used for high-throughput multiplexed microRNA analysis [11] but rely on a rather complex optical measurement setup. Optical biosensors using grating nanostructures (photonic-crystal slabs) are easily interfaced with out-of-plane incident light and particularly advantageous for multiplex measurements [12–15]. Usually, the wavelength shift of the quasi-guided mode resonance (GMR) in the transmission or reflection spectrum is detected upon refractive index changes on the nanostructure surface (Fig. 1(g)). Alternatively, the resulting intensity shift is measured by a detector [16–18]. A lower LOD was demonstrated by detecting the phase shift of the GMR (Fig. 1(g)) [19–21]. The interferometric setup increases the complexity of the system [19,21] and so far, only the analysis of one molecular biomarker has been demonstrated [19–21]. Mach-Zehnder-interferometers require beam splitters and mirrors [19] or electro-optical heterodyne interferometers are built with lock-in amplifiers and function generators [21]. Here, we introduce a new type of compact common-path interferometer biosensor using a multi-pinhole aperture and suitable for simultaneous sampling of tens of measurement fields for multiplex

molecular biomarker detection. The pinhole based common path interferometer just relies on apertures and a circular polarizers, additional to the common optical components such as lenses and the light source.

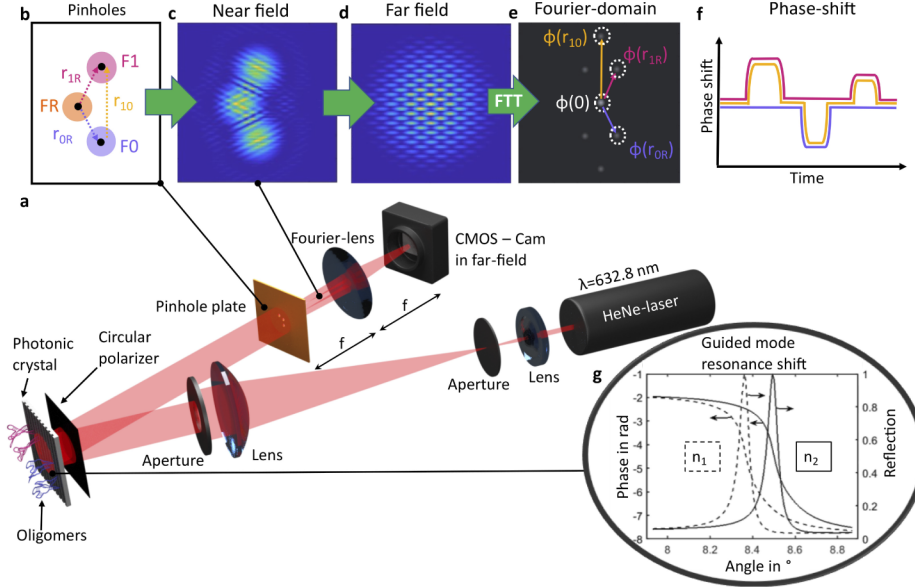


**Fig. 1.** Multi-pinhole Fourier frequency division method and setup. a) Common-path interferometer setup for measurement of proteins binding to a photonic-crystal surface functionalized with oligomers. Using a multi-pinhole plate and a Fourier lens the far field interference pattern is obtained on the camera. b) Example 3-pinhole pattern (black spots) sampling measurement fields F0, F1 and FR. c) Near field diffraction pattern (Fourier transform of wavefront in pinholes), and d) far field diffraction pattern (Fourier transform of wavefront in pinholes), and e) inverse Fourier transform of the far field intensity. f) Phase shift signals from different complex frequencies in the Fourier domain are measured to detect a refractive index change on the functionalized surface. g) Reflection intensity and phase shift of the transverse magnetic GMR upon analyte refractive index change from  $n_1$  to  $n_2$ .

## 2. Methods and materials

### 2.1. Mathematical description of the far field and phase calculation

The far field pinhole diffraction pattern and its Fourier Transform are mathematically expressed as follows [22,23]. The optical fields within the pinholes are defined as:

$$E_n = A_n e^{i\phi_n} \quad (1)$$

They depend on their phase  $\phi_n$  and amplitude  $A_n$ . Hence, the total field produced by the N-pinhole pattern is:

$$E = \sum_{n=1}^N E_n \text{circ}(x - x_n, y - y_n) = t(x, y) \quad (2)$$

The circular pinhole area at the position  $(x_n, y_n)$  is defined by the circ() function. The intensity of the far field diffraction pattern is calculated by the Fourier transform  $\mathcal{F}$ :

$$I(X, Y) = I_0 \left| \sum_{n=1}^N E_n \mathcal{F} \{ \text{circ}(x - x_n, y - y_n) \} \right|^2 \quad (3)$$

The intensity is recorded by a camera. To demodulate and decompose the pattern into its frequency components for the phase calculation, the inverse Fourier transform is applied:

$$g(u, v) = \mathcal{F}^{-1}\{I(X, Y)\} = \iint t(X, Y) * t^*(X - u, Y - v) dXdY \quad (4)$$

$$= \sum_{m=1}^N \sum_{n=1}^N A_m A_n e^{i(\phi_m - \phi_n)} \iint \text{circ}(X - x_m, Y - y_m) \text{circ}(X - u - x_n, Y - v - y_n) dXdY \quad (5)$$

$$= \sum_{m=1}^N \sum_{n=1}^N P_{mn}(u, v) E_m E_n^* \quad (6)$$

Thereby  $P_{mn}(u, v)$  is the convolution of the  $m^{\text{th}}$  with the  $n^{\text{th}}$  pinhole. The phase difference  $\phi_{mn} = \phi_m - \phi_n$  is calculated by:

$$\phi_{mn}(u, v) = \tan^{-1} \left( \frac{\Im(g(u, v))}{\Re(g(u, v))} \right) \quad (7)$$

## 2.2. Photonic-crystal fabrication

A photonic-crystal grating is replicated from a quartz-glass master that has a grating structure of 370 nm and a grating depth of 45 nm (203104.1, AMO GmbH). The master is placed into a mold with polydimethylsiloxane (PDMS, Sylgard DC 184 A&B, Biesterfeld Spezialchemie GmbH) and then baked for 30 min. After the PDMS is hardened, the PDMS replica is removed from the glass master. The PDMS grating is used as a stamp to transfer the grating nanostructure into a 200 nm thick AMONIL (Amonil MMS4, AMO GmbH) layer. At first AMOPRIME (AMOPRIME, AMO GmbH) is spin-coated onto a cleaned glass substrate at 3000 rpm for 30 s. Then it is placed on a hotplate for 2 min at 110°C and cooled down for another 2 min. On top an AMONIL layer is spin-coated with 3000 rpm for 30 s. Then the grating structure is placed onto the AMONIL layer and gently pressed into it. To develop the AMONIL layer it is illuminated with UV light. The PDMS stamp is removed and a Nb<sub>2</sub>O<sub>5</sub> is sputtered onto the grating as a high index layer.

## 2.3. Optical measurement setup

The optical measurement setup is shown in Fig. 1(a). As a light source a HeNe laser (Thorlabs, HNL008L) with a center wavelength of 632.8 nm is used. Followed by an aspheric focusing lens with  $f = 4.6$  mm and a collimating lens with  $f = 150$  mm aligned as a telescope setup to magnify the collimated laser beam. An adjustable aperture is used to change the spot size of the magnified beam on the photonic crystal. In front of the photonic crystal a circular polarizer is placed to prevent reflection of the laser beam at the air-glass interface at the backside of the photonic crystal. The photonic crystal is placed within a microfluidic chamber made of rubber and glass (Fig. 2). The nanostructure lies within the fluidic chamber and the photonic-crystal slab is illuminated from its backside. The scattered GMR light passes through the circular polarizer and the pinholes. The pinholes have a diameter of 400  $\mu\text{m}$  and a short distance of 1.4 mm and 2.6 mm for the long distance. They select GMR light from specific regions of interests on the photonic-crystal slab (Fig. 1(b)) and diffract the light onto a CMOS camera DCC1545M which records frames of the near field (Fig. 1(c)). Alternatively, a Fourier lens is placed between the pinhole aperture and the camera to record the far field diffraction pattern (Fig. 1(d)). The pinhole aperture and camera are in the front- and back-focal plane of the Fourier lens. The photonic crystal in the microfluidic chamber is placed on a rotation stage to adjust the angle of incident  $\alpha$  to match the angle of resonance for the laser wavelength  $\lambda_{\text{res}}$  and the photonic crystal grating period of  $\Lambda = 370$  nm according to the Bragg theory ( $\lambda_{\text{res}} = \Lambda(n_{\text{eff}} \pm \sin(\alpha))$ ). The angle depends on the effective refractive index  $n_{\text{eff}}$  of the guided mode.

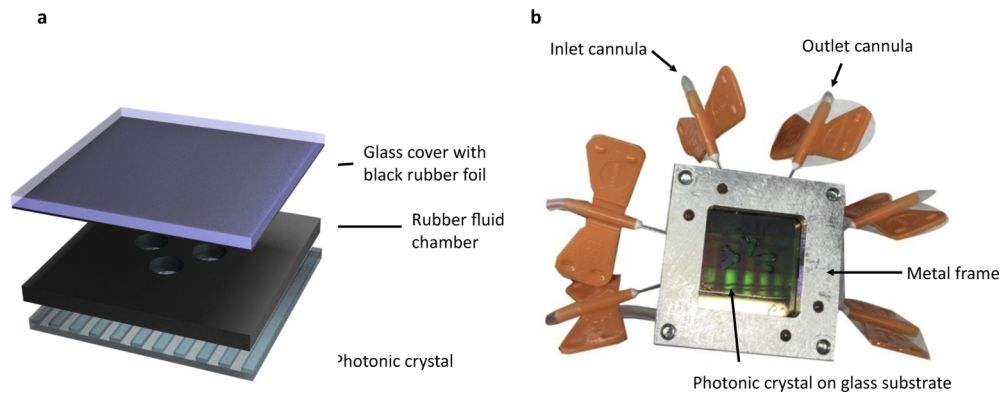


**Fig. 2.** Fluidic chamber design. a) 3-chamber design between photonic crystal slab and glass cover. b) Photonic crystal in fluid chamber with infusion set needles and tubes as in- and outlets.

#### 2.4. Fluidic chamber fabrication

The chamber is fabricated out of a 2 mm thick rubber foil. The foil is cut into a square of size 2 mm  $\times$  2 mm. To form fluidic chambers holes with a diameter of 1.5 mm are punched into the foil with a biopsy punch. The rubber foil with the chambers are fixed in between two glass substrates. One with the photonic crystal on the inside and one plain glass substrate as cover. Latter is covered with a black rubber foil to reduce reflections (Fig. 2(a)). The glass substrates are held together by a custom-made sample holder consisting of two metal frames and screws. As in- and outlets, cannulas from an infusion set are punched through the rubber into the chambers (Fig. 2(b)). For the thrombin binding measurement, a single fluid chamber design is used and for the bulk refractive index measurement a three-chamber design

#### 2.5. Biofunctionalization

The thrombin binding oligomers and their immobilized protocol are described in [13].

#### 2.6. Image processing

The recorded image frames are processed by a python script to calculate the phase as a function of time for each interference spot of interest. For each frame, the Fast Fourier Transform is calculated. The phase is unwrapped to prevent phase jumps and allow a continuous phase change. A moving average filter with a box size of 11 frames is used to reduce noise.

#### 2.7. Numeric calculations

The reflectance of the guided mode resonance and its phase in Fig. 1(g) are calculated with the finite element (FEM) simulation software COMSOL. The two-dimensional model (see Supplement 1) consists of one unit cell of the photonic crystal with a grating period of 370 nm and grating depth of 45 nm. The model is built up by three different material layers – a substrate AMONIL layer, a 115 nm thick  $\text{Nb}_2\text{O}_5$  high index layer on top of the grating and a water layer. At the top and bottom of the material stack perfectly matched layers are added with a perfect conductor as boundary condition. At the sides of the unit cell, a Floquet periodic boundary condition is applied. To simulate a bulk refractive index shift the refractive index of water is modified. Within the AMONIL layer a port is placed to excite the photonic crystal and to measure the scattering parameters and reflection. To measure the transmission a second port is added within the water layer. The optical near and far field diffraction patterns were computed with MATLAB.

The far field is computed based on the input field defined by the pinhole pattern and the 2D Fast Fourier transform. The near field is calculated based on the Fresnel approximation using a numerical approach [24] based on the 2D Fast Fourier transform FFT2 and its inverse invFFT2. The calculation is based on the input field  $U_0$ , the wavelength  $\lambda$ , the wavevector  $k$ , the propagating distance between the pinholes and the plane of observation  $z$  and the FD coordinates  $u$  and  $v$ :  $\text{invFFT2}\{\text{FFT2}\{U_0\}e^{ikz}e^{-i\pi\lambda z(u^2+v^2)}\}$ .

### 3. Results

#### 3.1. Multi-pinhole Fourier frequency-division multiplexing

The key element is the multi-pinhole aperture, placed into the reflected transverse magnetic GMR light originating from a photonic-crystal slab (Fig. 1(a,b)). The principle is related to multi-pinhole interferometry used for probing the orbital angular momentum of optical vortices [22,23] or the angular momentum of light in astrophysics [25,26]. The pinholes spatially select parts of the wavefront (Eq. (2)) and diffract GMR light into the near and far field (Eq. (3)). The pinholes are arranged relative to the photonic-crystal surface such that they select light from specific measurement (F0,F1) and reference (FR) sites (Fig. 1(b)). The diffracted light overlaps and results in an interference pattern (Fig. 1(c,d)). A relative phase change between two sites results in a phase change of the interference pattern produced by the pinholes (Eq. (5)). Hence, the measurement signals are modulated onto the spatial carrier frequencies of the pinhole pattern. The signal can be reconstructed by measuring the near field interference pattern that is mathematically the Fresnel transform of the selected wavefront parts with a camera and subsequent computation (Fig. 1(c), see Supplement 1). Alternatively, a Fourier lens is placed in front of the camera to record the far field intensity that is the Fourier transform (Fig. 1(d), Supplement 1). Calculating the Fast-Fourier-transform (FFT) of the far field camera image separates the superimposed frequencies spatially in the Fourier domain. The magnitude of the complex values is shown in Fig. 1(e). Each frequency spot is proportional to the convolution of the field amplitudes from two pinholes. Its complex amplitude contains the phase difference between the two pinholes (Eq. (5)). Their position in the Fourier domain is determined by the spatial vector  $r_{nm}$  between the two pinholes  $n$  and  $m$ . Knowing the pattern of pinholes allows to select the right frequencies in the Fourier domain to calculate the relative phase difference  $\phi_{nm}(r_{nm})$  between two fields on the photonic-crystal slab (Eq. (7)). Due to the demodulation of the carrier frequencies in the Fourier domain, we call the method Fourier frequency division multiplexing (FFM). Tracking the phase over time results in a phase shift graph as shown in Fig. 1(f). Light source flicker and environmental noise are common signals in the reference and measurement locations (assuming sufficiently small overall size and surface homogeneity). This implies self-referencing and noise cancellation.

#### 3.2. Pinhole pattern

The pinhole patterns must be designed such that the resulting frequencies in the Fourier domain do not overlap. This is fulfilled by an odd number  $N$  of pinholes equidistantly aligned on a circle with radius  $r_C$  [22]. As an example, Fig. 3(a) shows a circular 11-pinhole pattern. The pinholes are labeled with  $B_x$  when the pinhole samples a biomarker measurement field and with  $R_y$  in case of a reference site. The Fourier transform of the far field diffraction pattern shows  $N^2 - (N - 1) = 111$  bright spots (Fig. 3(c)). Each has a cone-shape intensity distribution (see Supplement 1). The center spot is the superposition of all autocorrelation parts ( $m = n$ ) with  $N$ -times the intensity of the other spots (see Supplement 1). The pinhole difference vector  $r_i$  with  $i \in \mathbb{N}$  determines the position vector in the Fourier domain. Hence, the inner frequency spots on the circle (Fig. 3(c)) with the smallest radius  $r_1$  are proportional to the convolution of pairs resulting from neighboring pinholes. To illustrate, two pinhole positions matching



two different biomarker binding sites  $B_1$  and  $B_2$  are colored in magenta and blue (Fig. 3(a)). Difference vectors between the biomarker pinholes and reference pinholes  $R_x$  are shown in the corresponding color. Knowing these vectors, the frequency positions of interest in the Fourier domain are located (Fig. 3(c)). All other biomarker-reference spot vectors not related to the two colored pinholes are shown in orange (Fig. 3(b)). The remaining spots in the Fourier domain in Fig. 3(b) correspond to the phase difference signal between two biomarker binding sites  $B_x$  and  $B_y$ . Also important are the phase shift signals between reference sites (grey) as they contain information about background noise. This example shows the wealth of information that may be extracted from the interference pattern to enhance the reliability of the measurement. The number of pinholes  $N$  with a given diameter  $d_{ph}$  aligned on a circle is limited. For a fixed circle radius  $r_C$ , with increasing  $N$  the radius  $r_i$  in the FD decreases as the pinhole distance in real space decreases too. At a certain point, the spots in the FD with the diameter  $2d_{ph}$  start to overlap. The limit of spot resolution in the FD is reached when the edge of one spot cuts the middle point (maximum) of the neighboring point. For large  $N$  the limit converges against  $N = \pi\sqrt{2r_C/d_{ph}}$  (Supplement 1). To double the number of pinholes with fixed pinhole diameter  $d_{ph}$  we would need to increase the radius  $r_C$  of the pinhole circle by a factor of 4. Additionally, to increase the number of measurement sites and their density, the distance of pinholes  $r_i$  can be increased by an increment of  $2d_{ph}$  after one circle with radius  $r_i$  is complete in the FD (Fig. 3(f)). To prevent overlapping the pinhole distance has to be smaller than  $2r_1$ . This leads to a spiral pattern (Fig. 3(d)). A spiral pattern with 54 pinholes and three different radii is shown in Fig. 3(d). Their pinhole diameter is  $30\ \mu\text{m}$ . There is less empty space in the middle than with a circular pattern that has the same number of pinholes and pinhole diameter. Such a circular pattern would have a minimum diameter  $2r_C$  of approximately 8.9 mm (Supplement 1). This is approximately 2.5 times larger than the diameter of the spiral pattern. Here, the referencing is proposed by nearest neighbor referencing and the inner three circles in the far field diffraction pattern (Fig. 3(e,f)) correspond to difference signals between two neighboring positions. The compactness of the pinhole-pattern design is achieved at the cost of partly overlapping interference positions between non-neighboring pinholes. Latter are positioned in the FD outside the circle with a radius of  $2r_1$ .

### 3.3. Multiplex measurements

To prove the suggested multiplexing method, a 3-pinhole pattern is used to experimentally measure the bulk refractive index change in two different fluidic chambers F0 and F1 in parallel, relative to a third reference chamber FR (Fig. 2). At the beginning all chambers are filled with water. Then the fluidic chambers F0 and F1 are filled with different ethanol/water concentrations (Fig. 4(e)) which possess slightly different refractive indices (see Supplement 1). Each time a fluid is injected into one of the measurement chambers, water is injected into the reference chamber too. The rubber fluidic chambers are attached to the photonic-crystal slab surface (colored areas in Fig. 3(a)), their centers are aligned concentrically to the position of the pinholes (colored small dots in Fig. 4(a)). The GMR light is diffracted by the pinholes. In the near field, an interference pattern is produced that is shown in the background of Fig. 3(a). The image is recorded by a camera and its computed FFT is shown in Fig. 3(b). The FFT of the recorded far field is shown in Fig. 3(c). It has high similarity to the theoretical computed image in Fig. 3(d). The relative phase shifts  $\phi(r_{0R})$ ,  $\phi(r_{1R})$  and  $\phi(r_{10})$  are calculated from the complex amplitudes at the spots representing the interference between the chambers F0-FR, F1-FR and F1-F0 respectively. The relative phase shift over time can be seen in Fig. 3(f). The phase shift behaves as expected from the injection table in Fig. 4(e). During analyte injection short phase difference peaks between the channel which has no analyte change and the reference channel that has an analyte injection is explained by the difference in pressure between their chambers. Table 1 shows the noise and phase shifts calculated from the phase difference signal between measurement and reference chambers. For each refractive index step a LOD is calculated by the formula: LOD

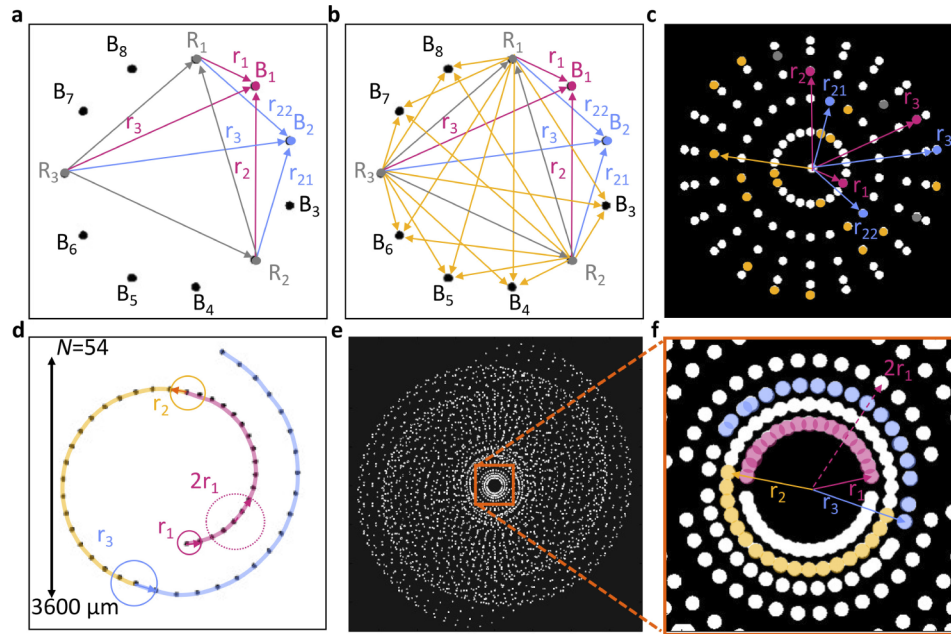


**Fig. 3.** Multiplex pinhole aperture designs. a) Design of circular 11-pinhole pattern matched to biomarker ( $B_x$ ) and reference ( $R_y$ ) measurement sites. The arrows indicate the difference vectors from the three reference spots to two exemplary biomarker spots  $B_1$  (magenta) and  $B_2$  (blue). Difference vectors between two references are shown in grey. b) Difference vectors between references and additional biomarker spots are shown in orange. c) The magnitude of the Fourier transform of the far field diffraction pattern of the circular pinhole pattern. The color of the frequency spots indicates the original pinhole pairs which produce the interference frequency (for better illustration a threshold is applied on the image). d) Spiral 54-pinhole pattern with three different radii. e) Magnitude of the Fourier transform of the far field diffraction pattern of the spiral 54-pinhole pattern with pinhole diameter 30  $\mu\text{m}$ . The center autocorrelation part is filtered out (for better illustration a threshold is applied on the image). f) Zoomed in center part of the FFT of the far field diffraction pattern (for better illustration a threshold is applied on the image).

$= 3\sigma/S$ . From the water to 3 % ethanol steps in chamber F1 an average LOD of  $4 \times 10^{-5}$  RIU is calculated. The noise is determined by the standard deviation  $\sigma$  of the stable phase signal before and after each refractive index step. Figure 5 shows exemplary the first 100 frames used to calculate the noise of the signal before the first refractive index step. It corresponds to a time of 2.8 minutes. The photonic crystal in the measurement chamber F1, has a maximum sensitivity of 420 rad/RIU for the water to 3 % ethanol step. The lower sensitivity calculated from the water to 10 % ethanol step in the same chamber is explained by the phase slope (Fig. 1(g)) that is only linear over a certain angle and wavelength range. Depending on the angle alignment and the amount of refractive index change the GMR can be shifted out of the linear range with a high phase slope and sensitivity. For phase shifts within the linear range, the FEM simulations show a sensitivity of 506 rad/RIU. The photonic crystal in chamber F0 has a lower sensitivity probably because its resonance position is at the edge of the linear slope due to inhomogeneities of the photonic-crystal slab layer thickness. In average, phase difference signals from chamber F1 have a noise of  $6.42 \times 10^{-3}$  rad. Partly, the high noise results from inhomogeneities in the photonic-crystal slab layer thickness and hence sensitivity differences between the interfering photonic-crystal slab areas. This limits the self referencing noise cancellation effect. Besides, the

main contribution to the noise arises from the thermo-optic effect. For example, a 21 % ethanol solution in water has a thermo-optic coefficient (TOC) of  $dn/dT = -1.66 \times 10^{-3} \text{ 1/K}$  at room temperature ( $25^\circ\text{C}$ ), whereas for water it is only  $dn/dT = -1.5 \times 10^{-4} \text{ 1/K}$  [27]. Assuming the reference chamber is filled with water and the measurement chamber with the ethanol solution, they would have a TOC difference of  $dn/dT = -1.5 \times 10^{-3} \text{ 1/K}$  when both perceive the same temperature fluctuation. Temperature fluctuations in the fluidic chamber are in the order of  $T = 0.005 \text{ K}$  under experimental conditions. For the maximum sensitivity, this corresponds to a phase shift of  $2.84 \times 10^{-3} \text{ rad}$ . In case of a relative temperature difference of  $T = 0.005 \text{ K}$  in addition, the temperature noise rises to  $3.6 \times 10^{-3} \text{ rad}$ . This explains the high noise level we observe. However, for protein binding experiments, in a one chamber design, with a HCl buffer solution and smaller pinhole distances, temperature fluctuations between a reference and measurement site are minimized. Due to smaller thickness inhomogeneities of the photonic crystal slab the sensitivity difference is reduced. Both are promising strategies to lower the noise and the LOD.

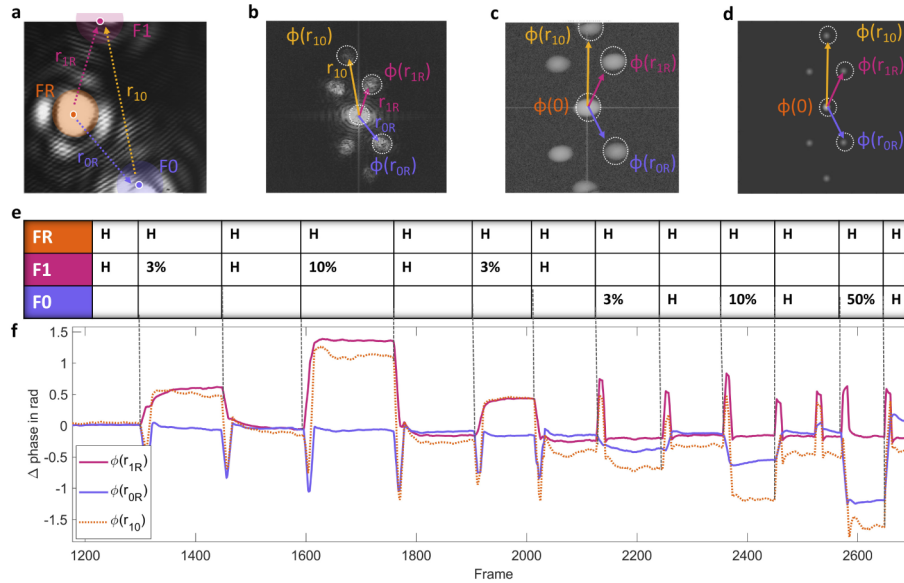


**Fig. 4.** Multiplex 3-field bulk refractive index measurement. a) Pinholes (colored small dots) projected onto the fluidic chambers. FR: Reference chamber, F0: Fluid chamber 0, F1: Fluid chamber 1. The arrows are the difference vectors between the pinholes. Background: Diffracted GMR light from the pinholes (near field). b) FFT of the measured near field interference pattern. The arrows indicate the position vectors of the complex frequencies. c) FFT of far field diffracted GMR light, measured with Fourier-lens. d) Computed far field diffraction pattern. e) Experimental fluid injection sequence. H: dH<sub>2</sub>O, x %: x vol% ethanol in dH<sub>2</sub>O. f) Phase signals from F0 and F1 fluid chambers relative to the reference chamber FR and relative to each other. The steps correspond to different ethanol/dH<sub>2</sub>O solutions with different refractive indices (see Supplement 1).

### 3.4. Binding of thrombin molecules

Thrombin-binding oligomers are immobilized on the photonic-crystal slab to validate that protein binding processes can be measured with the setup. The phase shift between a functionalized and non-functionalized reference site is evaluated. To produce a temporal phase signal, different thrombin concentrations in HCl buffer are injected into the fluidic chamber in a specific sequence



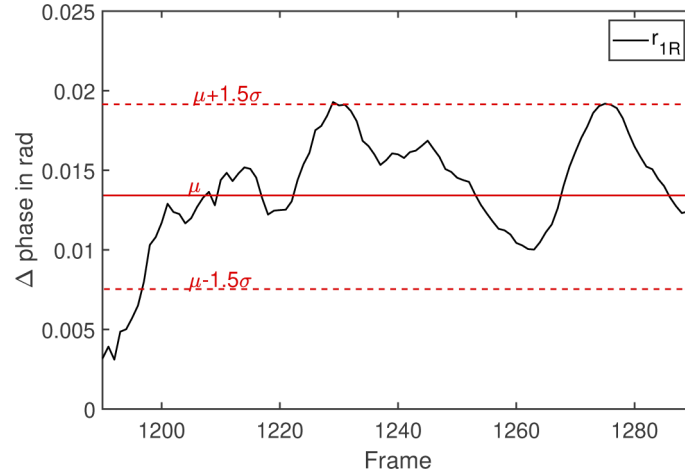


**Fig. 5.** Noise from chamber F1 during the multiplex bulk refractive index measurement. The phase signal median  $\mu$  is shown together with the range of three times the standard deviation  $\sigma = 3.4 \times 10^{-3}$  around the median.  $\sigma$  is used to quantify the noise of the signal. The 100 frames cover a time of 2.8 minutes.

**Table 1.** Refractive indices  $n$  and phase shifts with noise levels, sensitivities and the limit of detection LOD calculated for each step. The noise and phase shifts are calculated from the phase difference signals between the measurement chambers F1/2 and the reference chamber FR

Ch.	Step in V%	$\Delta n$ in RIU	Noise pre-step in rad $\times 10^{-3}$	Noise post-step in rad $\times 10^{-3}$	Noise combined in rad $\times 10^{-3}$	Phase shift rad	Sensitivity in rad/RIU	LOD in RIU $\times 10^{-5}$
F1	0 – 3	$1.43 \times 10^{-3}$	3.4	9.7	6.55	0.6	420	4.68
F1	0 – 10	$5.17 \times 10^{-3}$	9.2	6.7	7.95	1.4	272	8.81
F1	0 – 3	$1.43 \times 10^{-3}$	5.00	4.5	4.75	0.6	420	3.4
F0	0 – 3	$1.43 \times 10^{-3}$	6.7	17.5	12.1	0.2	140	26
F0	0 – 10	$5.17 \times 10^{-3}$	2.9	2.25	1.27	0.5	97	39.4
F0	0 – 50	$2.82 \times 10^{-2}$	16.3	12.4	14.4	1.1	39	110

(Fig. 6). The resulting phase shift signal follows the typical association and dissociation binding dynamic of thrombin binding oligomers [28]. To regenerate the sensor, the fluidic chamber is rinsed with a 3 % NaCl in water solution to remove the thrombin molecules from the oligomers. Depending on the thrombin concentration the speed of binding and phase shift differs. The baseline level of the pure HCl buffer solution shows a signal drift over time. A minimum concentration of 76 nM (2.3 ug/ml) is detected and results in a strong phase shift. The signal is still rising and is not saturated when the sensor is regenerated with the NaCl solution at the end of the measurement. Due to the binding dynamic the phase difference rises as long as there is thrombin left in the buffer solution and the oligomers which bind thrombin on the surface are not saturated. Hence, the system has the potential to measure lower thrombin concentrations.

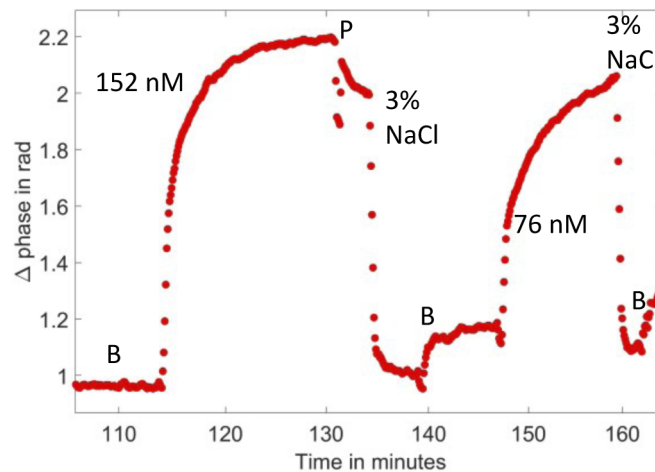


**Fig. 6.** Thrombin binding dynamics. Phase shift signal between a thrombin-binding oligomer site and a reference site for different thrombin concentrations. B: HCl buffer. 152 nM: 152 nM thrombin in HCl buffer. 76 nM: 76 nM thrombin in HCl buffer. 3 % NaCl: 3 % NaCl in dH<sub>2</sub>O.

#### 4. Conclusion

In summary, we introduced a new method for multiplex phase-detection biosensing with optical transducer elements such as photonic-crystal slabs. The key element is a pinhole pattern that modulates the phase difference between various measurement sites onto different spatial carrier frequencies. Circular and spiral pinhole patterns with up to 54 pinholes are shown. Based on this concept, multiplex bulk refractive index and protein binding experiments validate the concept. Applied to photonic-crystal biosensors the method combines the advantage of a compact system design with the potential of a low LOD, low sample volume, and intrinsically high-redundancy referencing.

**Acknowledgments.** The sputtering of the Nb<sub>2</sub>O<sub>5</sub> high index layer was done by Richard Marquardt and Finn Zahari from the Chair of Nanoelectronics at the Institute of Electrical Engineering and Information Technology, Kiel University.

**Disclosures.** The authors declare no conflicts of interest.

**Data Availability.** Data underlying the results presented in this paper are not publicly available at this time but are obtained from the authors upon reasonable request.

**Supplemental document.** See [Supplement 1](#) for supporting content.

#### References

1. D. W. Bates, D. Levine, A. Syrowatka, M. Kuznetsova, K. J. T. Craig, A. Rui, G. P. Jackson, and K. Rhee, "The potential of artificial intelligence to improve patient safety: a scoping review," *npj Digit. Med.* **4**(1), 54–58 (2021).
2. H. Haick and N. Tang, "Artificial intelligence in medical sensors for clinical decisions," *ACS Nano* **15**(3), 3557–3567 (2021).
3. K. Björkman, S. Jalkanen, M. Salmi, H. Mustonen, T. Kaprio, H. Kekki, K. Pettersson, C. Böckelman, and C. Haglund, "A prognostic model for colorectal cancer based on cea and a 48-multiplex serum biomarker panel," *Sci. Rep.* **11**(1), 4287 (2021).
4. J. F. Rusling, C. V. Kumar, J. S. Gutkind, and V. Patel, "Measurement of biomarker proteins for point-of-care early detection and monitoring of cancer," *Analyst* **135**(10), 2496–2511 (2010).
5. J. R. Sempionatto, M. Lin, L. Yin, K. Pei, T. Sonsa-ard, A. N. de Loyola Silva, A. A. Khorshed, F. Zhang, N. Tostado, and S. Xu, "An epidermal patch for the simultaneous monitoring of haemodynamic and metabolic biomarkers," *Nat. Biomed. Eng.* **2021**, 1–12 (2021).
6. S. Punj, D. Sidhu, D. Bhattacharya, M. Wang, and P. K. Wong, "An electrochemical biosensor platform for rapid immunoanalysis of physiological fluids," *IEEE Open J. Nanotechnol.* **1**, 31–37 (2020).
7. Z. Hao, Y. Pan, W. Shao, Q. Lin, and X. Zhao, "Graphene-based fully integrated portable nanosensing system for on-line detection of cytokine biomarkers in saliva," *Biosens. Bioelectron.* **134**, 16–23 (2019).
8. S. J. Park, O. S. Kwon, S. H. Lee, H. S. Song, T. H. Park, and J. Jang, "Ultrasensitive flexible graphene based field-effect transistor (fet)-type bioelectronic nose," *Nano Lett.* **12**(10), 5082–5090 (2012).
9. J. Duffy, F. Padovani, G. Brunetti, P. Noy, U. Certa, and M. Hegner, "Towards personalised rapid label free mirna detection for cancer and liver injury diagnostics in cell lysates and blood based samples," *Nanoscale* **10**(26), 12797–12804 (2018).
10. P. Chen, M. T. Chung, W. McHugh, R. Nidetz, Y. Li, J. Fu, T. T. Cornell, T. P. Shanley, and K. Kurabayashi, "Multiplex serum cytokine immunoassay using nanoplasmonic biosensor microarrays," *ACS Nano* **9**(4), 4173–4181 (2015).
11. A. J. Qavi, J. T. Kindt, M. A. Gleeson, and R. C. Bailey, "Anti-dna: Rna antibodies and silicon photonic microring resonators: increased sensitivity for multiplexed microrna detection," *Anal. Chem.* **83**(15), 5949–5956 (2011).
12. G. Pitruzzello and T. F. Krauss, "Photonic crystal resonances for sensing and imaging," *J. Opt.* **20**(7), 073004 (2018).
13. S. Jahns, M. Bräu, B.-O. Meyer, T. Karrock, S. B. Gutekunst, L. Blohm, C. Selhuber-Unkel, R. Buhmann, Y. Nazirizadeh, and M. Gerken, "Handheld imaging photonic crystal biosensor for multiplexed, label-free protein detection," *Biomed. Opt. Express* **6**(10), 3724–3736 (2015).
14. S. Fan and J. D. Joannopoulos, "Analysis of guided resonances in photonic crystal slabs," *Phys. Rev. B* **65**(23), 235112 (2002).
15. G. Quaranta, G. Basset, O. J. Martin, and B. Gallinet, "Recent advances in resonant waveguide gratings," *Laser Photonics Rev.* **12**(9), 1800017 (2018).
16. Y. Nazirizadeh, U. Bog, S. Sekula, T. Mappes, U. Lemmer, and M. Gerken, "Low-cost label-free biosensors using photonic crystals embedded between crossed polarizers," *Opt. Express* **18**(18), 19120–19128 (2010).
17. Y.-C. Lin, W.-H. Hsieh, L.-K. Chau, and G.-E. Chang, "Intensity-detection-based guided-mode-resonance optofluidic biosensing system for rapid, low-cost, label-free detection," *Sens. Actuators, B* **250**, 659–666 (2017).
18. A. Drayton, K. Li, M. Simmons, C. Reardon, and T. F. Krauss, "Performance limitations of resonant refractive index sensors with low-cost components," *Opt. Express* **28**(22), 32239–32248 (2020).
19. P. K. Sahoo, S. Sarkar, and J. Joseph, "High sensitivity guided-mode-resonance optical sensor employing phase detection," *Sci. Rep.* **7**(1), 7607 (2017).
20. I. Barth, D. Conteduca, C. Reardon, S. Johnson, and T. F. Krauss, "Common-path interferometric label-free protein sensing with resonant dielectric nanostructures," *Light: Sci. Appl.* **9**(1), 96–99 (2020).
21. W.-K. Kuo, N.-C. Huang, H.-P. Weng, and H.-H. Yu, "Tunable phase detection sensitivity of transmitted-type guided-mode resonance sensor in a heterodyne interferometer," *Opt. Express* **22**(19), 22968–22973 (2014).
22. G. X. Wei, Y. Y. Liu, S. G. Fu, and P. Wang, "Measurement of fractional optical vortex by a ring-type multi-pinhole interferometer," in *Advanced Materials Research*, vol. 433 (Trans Tech Publ, 2012), pp. 6339–6344.
23. M. R. Dennis and J. B. Götte, "Topological aberration of optical vortex beams: determining dielectric interfaces by optical singularity shifts," *Phys. Rev. Lett.* **109**(18), 183903 (2012).
24. D. P. Kelly, "Numerical calculation of the fresnel transform," *J. Opt. Soc. Am. A* **31**(4), 755–764 (2014).
25. C.-S. Guo, S.-J. Yue, and G.-X. Wei, "Measuring the orbital angular momentum of optical vortices using a multipinhole plate," *Appl. Phys. Lett.* **94**(23), 231104 (2009).
26. G. C. Berkhout and M. W. Beijersbergen, "Method for probing the orbital angular momentum of optical vortices in electromagnetic waves from astronomical objects," *Phys. Rev. Lett.* **101**(10), 100801 (2008).
27. S. Novais, M. S. Ferreira, and J. L. Pinto, "Determination of thermo-optic coefficient of ethanol-water mixtures with optical fiber tip sensor," *Opt. Fiber Technol.* **45**, 276–279 (2018).
28. J.-Y. Byeon and R. C. Bailey, "Multiplexed evaluation of capture agent binding kinetics using arrays of silicon photonic microring resonators," *Analyst* **136**(17), 3430–3433 (2011).